The role of strain hardening in the transition from dislocation-mediated to frictional deformation of marbles within the Karakoram Fault Zone, NW India

David Wallis[1]*, Geoffrey E. Lloyd[2] and Lars N. Hansen[1]

[1]*Department of Earth Sciences, University of Oxford, Oxford, UK, OX1 3AN,*

David.Wallis@earth.ox.ac.uk

[2]*School of Earth and Environment, University of Leeds, Leeds, UK, LS2 9JT.*

**Corresponding author*

Keywords

Calcite; Schmid factor; resolved shear stress; strain hardening; seismogenesis; Karakoram Fault Zone

Abstract

The onset of frictional failure and potentially seismogenic deformation in carbonate rocks undergoing exhumation within fault zones depends on hardening processes that reduce the efficiency of aseismic dislocation-mediated deformation as temperature decreases. However, few techniques are available for quantitative analysis of dislocation slip system activity and hardening in natural tectonites. Electron backscatter diffraction maps of crystal orientations offer one such approach *via* determination of Schmid factors, if the palaeostress conditions can be inferred and the critical resolved shear stresses of slip systems are constrained. We analyse calcite marbles deformed in simple shear within the Karakoram Fault Zone, NW India, to quantify changes in slip system activity as the rocks cooled during exhumation. Microstructural evidence demonstrates that between ~300°C and 200–250°C the dominant deformation mechanisms transitioned from dislocation-mediated flow to twinning

and frictional failure. However, Schmid factor analysis, considering critical resolved shear stresses for yield of undeformed single crystals, indicates that the fraction of grains with sufficient resolved shear stress for glide apparently increased with decreasing temperature. Misorientation analysis and previous experimental data indicate that strain-dependent work hardening is responsible for this apparent inconsistency and promoted the transition from dislocation-mediated flow to frictional, and potentially seismogenic, deformation.

1. Introduction

Calcite exhibits marked velocity-weakening behaviour, which may promote nucleation of unstable earthquake ruptures (Han *et al*., 2010; Verberne *et al*., 2015; Cowie *et al*., 2017). Faults hosted in calcite-rich lithologies are therefore major sources of seismic hazard in zones of active continental deformation (Smith *et al*., 2011). The depth extent of earthquake nucleation in such faults broadly corresponds to the depth at which the activity of temperature-dependent aseismic creep processes can prevent unstable frictional failure under interseismic strain rate conditions (Scholz, 1988; Verberne *et al*., 2015). Dislocation-mediated deformation mechanisms (potentially including contributions from dislocation creep, low-temperature plasticity, and/or dislocation-accommodated grain boundary sliding) are commonly inferred to have operated in calcite-rich shear zones exhumed from mid-crustal depths and in which the grain size and/or conditions were unfavourable for efficient diffusion creep (e.g. Bestmann *et al*., 2006; Rutter *et al*., 2007; Wallis *et al*., 2013; Parsons *et al*., 2016). Therefore, competition between dislocation-mediated flow and frictional failure may exert an important control on the depth limit of earthquake nucleation. However, the precise microphysical processes that control this transition in natural fault zones remain poorly constrained, particularly in situations where rocks are progressively exhumed during deformation, resulting in a transition from aseismic flow to potentially seismogenic frictional failure within the exhuming rock mass (Handy *et al*.,

2007). The strength of rocks undergoing dislocation-mediated deformation is a function of the stresses required to activate dislocation glide on particular crystallographic slip systems, which may depend on both environmental conditions (e.g. temperature, pressure, and strain rate) and other state variables (e.g. composition, dislocation density and distribution) (e.g., Hobbs *et al*., 1972; de Bresser and Spiers, 1997). However, it is challenging to determine the strength and activity of slip systems during dislocation-mediated deformation in natural tectonites, and relatively few techniques are available to do so. As a result, the precise controls on the transition from aseismic creep to frictional failure and potentially seismogenic behaviour in natural fault zones remain poorly constrained.

The most common approach to assess the relative activity of different slip systems in natural tectonites is to interpret the slip system(s) most likely to have generated an observed crystallographic preferred orientation (CPO); for example, by determining the slip system inferred to have most readily rotated into orientations with high resolved shear stress (e.g., Toy *et al*., 2008). However, such analysis is often limited to qualitative interpretations and comparisons. More quantitative information can be gleaned by comparing natural and experimental CPOs to results from simulations of polycrystal plasticity (e.g. Wenk *et al*., 1987). However, this approach tends to place relatively loose constraints on slip system activity due to the large parameter space that needs to be searched (i.e., typically many combinations of slip system strengths and deformation geometries have to be tested) and challenges in comparing natural and simulated CPO geometries quantitatively.

Another approach is to analyse crystallographic misorientations resulting from the presence of dislocations within grains (Lloyd *et al*., 1997; Bestmann and Prior, 2003; Wheeler *et al*., 2009). However, due to the limited angular resolution of commonly available measurement techniques (e.g. ~0.2° for misorientation angles from conventional electron

backscatter diffraction, EBSD) such analysis can only sample the fraction of the dislocation population that is arranged into relatively high misorientation substructures such as subgrain boundaries (Prior, 1999). As such, 'free' dislocations that are not in subgrain boundaries can be difficult to detect and generally require higher precision and more computationally expensive techniques such as high-angular resolution electron backscatter diffraction (Wallis *et al*., 2016a, 2017). Moreover, it is unclear to what extent the measured dislocation content was glissile or sessile during deformation. This ambiguity also often applies to direct observation of dislocations, by transmission-electron imaging, chemical etching, or decoration by oxidation.

In this contribution, we exploit advances in EBSD (Prior *et al*., 1999, 2009; Bachmann *et al*., 2010; Mainprice *et al*., 2011) to develop a method of slip system analysis based on determination of Schmid factors (Schmid, 1928; Schmid and Boas, 1950; Farla *et al*., 2011; Hansen *et al*., 2011). The Schmid factor of a slip system quantitatively describes the relation between resolved shear stress and applied stress state (the higher the Schmid factor, the greater the resolved shear stress on the slip system). This orientation relationship is typically qualitatively inferred when interpreting slip systems that contribute to CPO development (e.g. Toy *et al*., 2008). However, the Schmid factor not only quantifies this relationship, but also allows for calculation of resolved shear stresses on each slip system, and enables mapping of grains that are (un)favourably oriented for dislocation glide. Relatively few geological studies have utilised detailed Schmid factor analysis. Most of these focussed on stress states associated with radially-symmetric shortening or extension (e.g. Ralser *et al*., 1991; Farla *et al*., 2011; Hansen *et al*., 2011), and to our knowledge, only two have considered simple shear, both focussed on quartz (Law *et al*., 1990; Toy *et al*., 2008).

To explore the capabilities of this approach, we conduct a detailed Schmid factor

analysis of calcite in marbles deformed within a shear zone of the Karakoram Fault Zone (KFZ), NW India (Figure 1). Calcite is particularly well suited for Schmid factor analysis because: (1) techniques are well established to infer palaeostress magnitudes and orientations (Turner, 1953; Rowe and Rutter, 1990) as well as metamorphic and deformation temperatures (Covey-Crump and Rutter, 1989; Burkhard, 1993) from calcite microstructures; (2) the critical resolved shear stresses (CRSSs) of calcite slip systems are experimentally constrained (De Bresser and Spiers, 1997); and (3) these CRSSs and the post-yield behaviour exhibit low strain rate sensitivity (stress exponents in the ranges 5.3–42.6 and 9.3–15.5, respectively) indicating near plastic (as opposed to strain rate-sensitive viscous) behaviour when deformed at differential stresses greater than approximately 30 MPa (Wang *et al*., 1996; De Bresser and Spiers, 1997). The marbles that we investigate have undergone a protracted deformation history during exhumation and cooling from upper amphibolite-grade conditions to near surface depths and occur in a fault zone that exhibits geomorphological evidence for M_w 7+ earthquakes during the Quaternary (Brown *et al*., 2002; Rutter *et al*., 2007; Wallis *et al*., 2013). We investigate the latter part of this history as the rocks were exhumed and cooled through the frictional-viscous transition zone (Wallis *et al*., 2013, 2015) and underwent a transition from aseismic flow to potentially seismogenic frictional failure (Rutter *et al*., 2007). In particular, we use Schmid factor analysis combined with other microstructural observations to test: (1) the manner in which slip system activity potentially varied under evolving temperature and stress conditions during exhumation, (2) the impact of strain hardening on slip system activity, and (3) how these factors affected the transition from crystal plastic to frictional and potentially seismogenic styles of deformation.

2. Geological Setting

The KFZ is a > 800 km long fault zone that strikes NW-SE and delineates the western margin of the Tibetan plateau, accommodating dextral displacement resulting from the India-

Asia collision (Figure 1). Along the central KFZ in NW India structures formed at and below lower amphibolite grade are unequivocally attributable to deformation within the KFZ, and record a sequence of fault rocks formed at progressively lower temperature due to ongoing deformation during exhumation (Phillips and Searle, 2007; Wallis *et al.*, 2013, 2015). We investigate marbles deformed within the Pangong strand of the KFZ, adjacent to the Pangong Transpressional Zone (PTZ) (Figure 1).

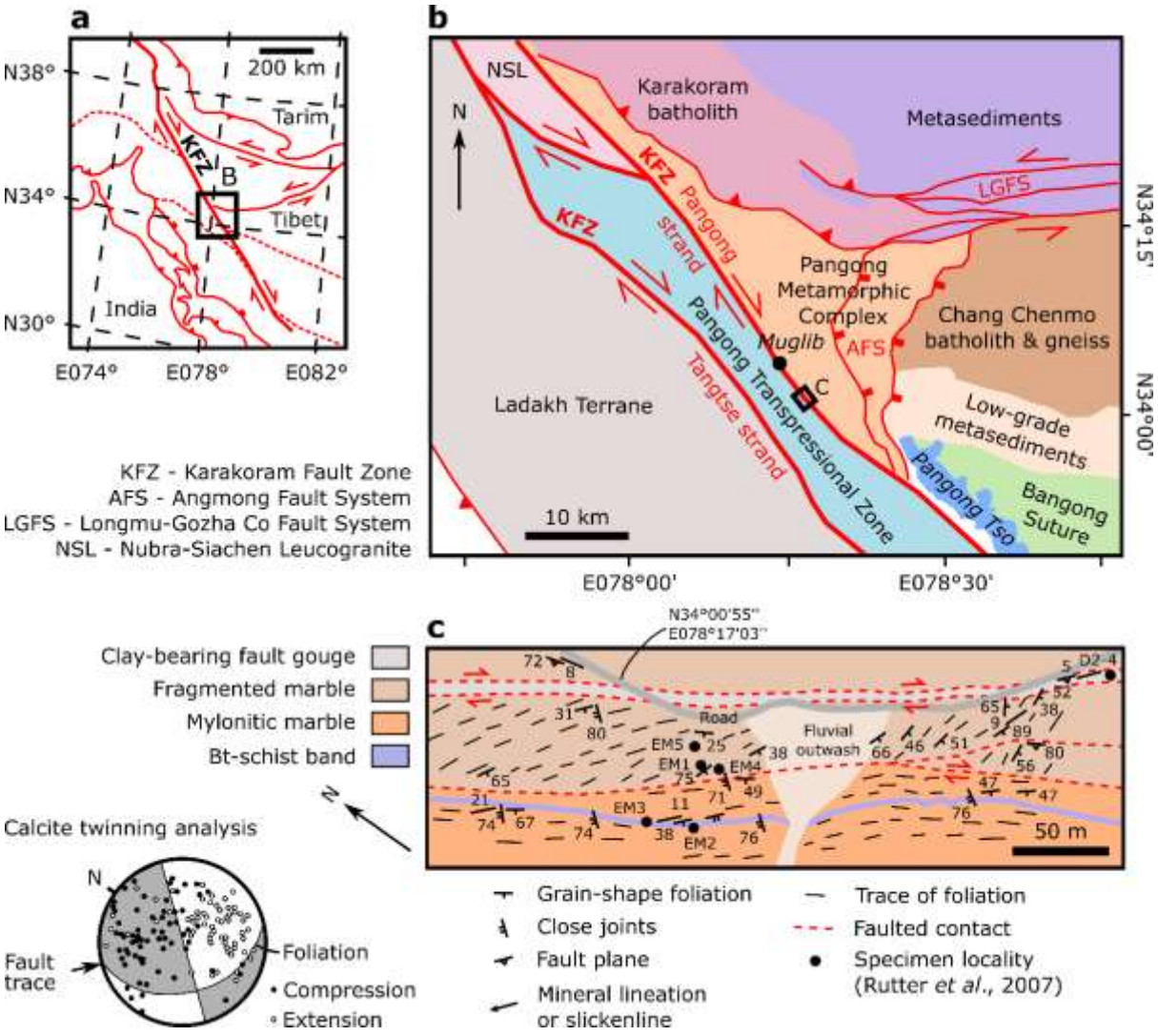

Figure 1

Simplified structural maps of the studied outcrop in the KFZ and wider tectonic context. (a) and (b) are drawn following Phillips and Searle (2007) and Van Buer et al., (2015). (c) is

modified from Rutter et al. (2007) and includes their specimen localities and the results of their calcite twinning analysis.

Between Muglib and Pangong Tso, the Pangong strand deforms rocks of the Pangong Metamorphic Complex (PMC) and juxtaposes them with the PTZ (Figure 1). The PMC consists of banded marbles, amphibolites, and pelites that underwent regional metamorphism under kyanite grade (up to 736 ± 47°C and 1059 ± 219 MPa, Wallis *et al*., 2014) and sillimanite grade conditions (Streule *et al*., 2009), followed by retrograde metamorphism and KFZ deformation under lower amphibolite to sub-greenschist conditions (Rutter *et* al., 2007; Streule *et al*., 2009; Wallis *et al*., 2014; Van Buer *et al*., 2015).

Rutter *et al*. (2007) studied in detail an outcrop of deformed marble near Muglib (N34°00'55'' E078°17'03''), providing the context for this study (Figure 1). Here we summarise the most relevant findings of their study. Grain-shape foliation at this locality dips moderately SW and mineral stretching lineations plunge gently both NW and SE, consistent with the wider KFZ kinematics. Rutter *et al*. (2007) investigated seven marble samples exhibiting microstructures that record mylonitic fabrics evident as varying degrees of dynamic recrystallisation. From the reconstructed grain size of weakly recrystallised host grains, they estimated metamorphic temperatures in the range 300 ± 20°C to 480 +130/-30°C, using the grain size-temperature relationship of Covey-Crump and Rutter (1989). These data place an upper limit on the temperature of overprinting deformation in each sample. The grain size of dynamically recrystallised neoblasts indicates flow stresses in the range of 40 ± 20 MPa to 110 ± 40 MPa according to the calibration of Rutter (1995) based on dynamic recrystallisation by grain boundary migration. The choice of this calibration, rather than an alternative based on dynamic recrystallisation by subgrain rotation (Rutter, 1995), is supported by our microstructural analysis in the following sections, which reveals irregular grain boundary morphologies but limited subgrain development, consistent with microstructures reported by

Rutter *et al.* (2007). Twin incidence (the percentage of grains, in a given grain size class interval, that contain optically visible twin lamellae) indicates differential stresses in the range of 160 ± 30 MPa to 250 ± 30 MPa according to the calibration of Rowe and Rutter (1990). Thick twins exhibit straight, or curved and tapered boundaries indicating temperatures of 200–250°C (Burkhard, 1993). These constraints, along with observations that the mylonitic fabric is cross-cut by calcite veins that are twinned but not mylonitised, suggest that twinning postdates dynamic recrystallisation (Rutter *et al.*, 2007). Dynamic analysis of calcite twins, using the method of Turner (1953), indicates a palaeostress state that exerted N-S compression and E-W extension, consistent with transpressional motion on the NW-SE-trending fault trace, foliation and lineations (Figure 1).

Table 1 *Microstructural data from calcite in EM1 and inferred deformation conditions experienced by sample EM1, from Rutter et al. (2007)*

Parameter	Value	Notes
Host grain size (μm)	240 ± 11	Measured from weakly recrystallised grains where the original grain outline could be established.
Dynamically recrystallised grain size (μm)	40 ± 9	Measured from digital maps of several hundred grains following Rutter (1995).
Overall (host and recrystallised) grain size (μm)	48 ± 10	Measured from digital maps of several hundred grains following Rutter (1995).
Temperature (°C)	310 ± 20	From grain size-temperature relationship of marbles on Naxos, Greece, based on Covey-Crump and Rutter (1989). Taken as an approximate upper-bound for the deformation temperature.
Flow stress (differential) (MPa)	98 ± 35	From dynamically recrystallised grain size using the calibration of Rutter (1995).
Twinning stress (differential) (MPa)	210 ± 30	From the twinning incidence piezometric relationship of Rowe and Rutter (1990).

The marbles at the Muglib locality are locally overprinted by bands of cataclasite and are cross-cut by a ~10 m thick zone of clay-bearing fault gouge that displays P foliations and R_1 Riedel shears consistent with dextral KFZ deformation (Figures 1 and 2). The Kübler index for authigenic illite in the gouge indicates gouge formation at the anchizone-epizone transition, tentatively taken to be ~300°C (Figure 2; Rutter *et al*., 2007). The overprinting of mylonitic textures by cataclastic textures records the transition from crystal plastic deformation of the marbles to frictional and potentially seismogenic deformation within the marble cataclasite and clay-rich gouge zone.

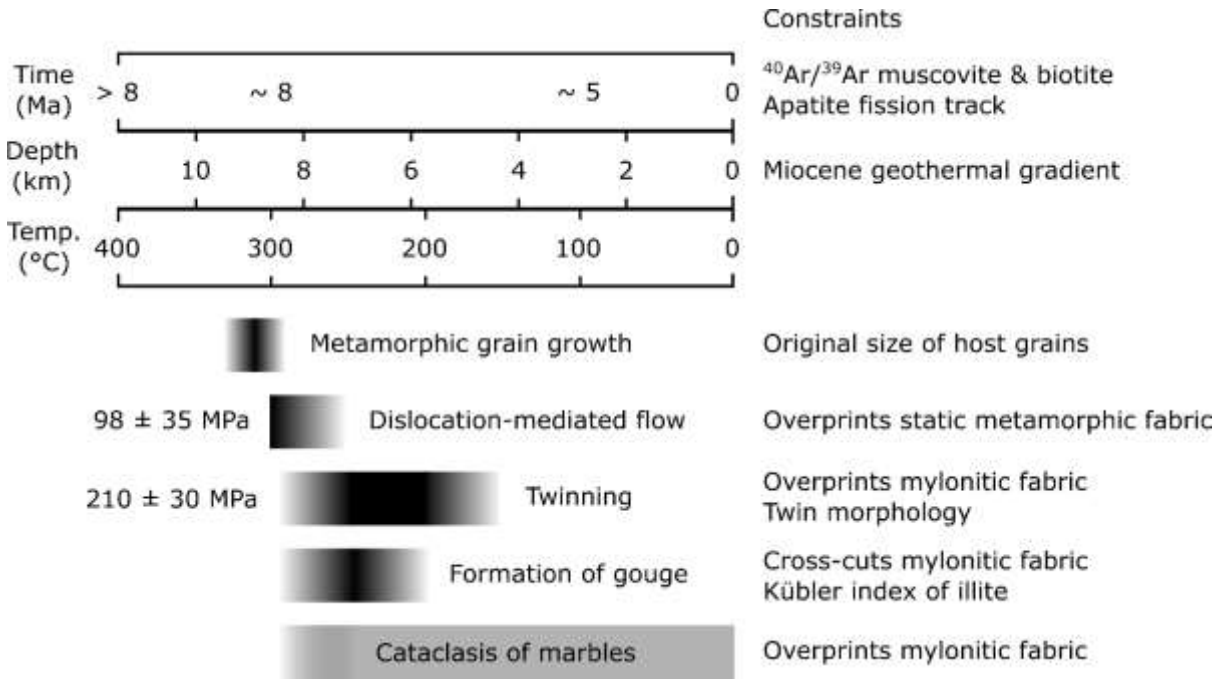

Figure 2 *Summary of constraints on the deformation and exhumation histories of the investigated marble sample EM1 (metamorphic grain growth, dislocation-mediated flow, and twinning) and the surrounding rocks (formation of gouge and cataclasis). Constraints on temperatures of deformation and metamorphic processes, along with differential stresses, are obtained or inferred from Rutter et al. (2007). The Miocene geothermal gradient within the Pangong Transpressional Zone was estimated by Wallis et al. (2014) to be ~35°C/km based on geothermobarometry of migmatites formed at ~17 Ma. Time constraints are derived from*

184 *$^{40}Ar/^{39}Ar$ and apatite fission track thermochronology (Boutonnet et al., 2012; Wallis et al,*
185 *2016b).*

186 Thermochronological data from biotite $^{40}Ar/^{39}Ar$ (Boutonnet *et al*., 2012) and apatite fission
187 track (Wallis *et al*., 2016b) indicate that the Pangong strand and PTZ cooled from ~320°C to
188 ~120°C between ~9 Ma to ~5 Ma (Figure 2). Dynamic recrystallisation of the marbles therefore
189 likely occurred at 7–9 Ma, and deformation twinning at ~6–7 Ma (Figure 2). Offset geological
190 markers indicate long-term average slip rates of 2.7–10.2 mm/yr since ~15 Ma (Phillips *et al*.,
191 2004).

192 Quaternary deformation on the Pangong strand is recorded by offset debris flows and
193 alluvial fans, which indicate an average slip rate of 4 ± 1 mm/yr since 11–14 ka (Brown *et al*.,
194 2002). These landforms are offset by several metres, indicating the occurrence of earthquakes
195 of > 7 M_w, with probable recurrence intervals of ~500–1000 years based on both the ages of
196 the landforms and earthquake scaling relationships (Brown *et al*., 2002; Wallis *et al*., 2013).
197 Brown *et al*. (2002) inferred that a 7 M_w earthquake has occurred on the Pangong strand since
198 1–2 ka.

199 For this study we focus on mylonitic marble sample EM1 of Rutter *et al*. (2007), for
200 which the deformation conditions are particularly well constrained (Table 1, Figure 2).
201 Notably, this is one of the lowest temperature samples studied by Rutter *et al*. (2007), with the
202 size of host grains placing an upper limit of 310 ± 20°C on the temperature of formation of the
203 mylonitic fabric (Table 2). This temperature is similar to the temperature of ~300°C estimated
204 for formation of the gouge layer. Therefore, EM1 records mylonitic deformation shortly
205 preceding, or broadly coincident with, the onset of frictional deformation at this structural level.
206 The results derived from detailed analysis of this sample are interpreted in the well-constrained
207 context, outlined above, of evolving deformation processes and conditions as the marbles and

surrounding units were exhumed.

3. Methods

A section of sample EM1 of Rutter *et al.* (2007) was cut parallel to the lineation and perpendicular to the foliation. This section was polished with successively decreasing grit sizes down to 0.25 µm diamond grit, followed by 0.03 µm colloidal silica. Electron backscatter diffraction (EBSD) data were collected on a band of fine-grained matrix calcite using an FEI Quanta 650 FEG E-SEM in the Department of Earth Sciences, University of Oxford. The system is equipped with an Oxford Instruments NordlysNano EBSD camera and AZtec/Channel5 software. Data were collected by automated mapping and consist of 1003 x 692 points with a step size of 1 µm. 96.9% of the map area was indexed as calcite, and the majority of points that were not indexed were due to the presence of other phases with rare occurrence, such as quartz. The data were processed to remove individual mis-indexed pixels that had > 10° misorientation from all their neighbours. Next, non-indexed pixels with ≥ 7 neighbours belonging to the same grain were filled with the average orientation of their neighbours. Maps of crystal orientation and local misorientation within a 3x3 pixel kernel were produced using Channel5. Pole figures and Schmid factor analyses were computed and plotted using the MATLAB® toolbox MTEX 4.5 (Bachmann *et al.*, 2010; Mainprice *et al.*, 2011). Analysis in MTEX utilised the built-in *SchmidFactor* function to operate on *slipSystem* and stress *tensor* MTEX objects (Supplementary Material). These objects were specified as the relevant slip systems for calcite and stress tensor for the natural deformation as described below.

The Schmid factor of a slip/twin system describes the fraction of the applied stress that is resolved onto a particular slip/twin plane in the slip/twin direction, and can be described either as a scalar value (Schmid, 1928; Schmid and Boas, 1950) or as a second rank tensor (e.g.

Pokharel *et al*., 2014). In the conventional definition, originally formulated for uniaxial tension (Schmid, 1928; Schmid and Boas, 1950), the Schmid factor (m^s) of a slip/twin system (s) is computed as

$$m^s = \cos\phi\cos\lambda, \quad (1)$$

where ϕ and λ are the angles between the maximum principal stress direction and the slip/twin plane normal and slip/twin direction, respectively. This scalar Schmid factor then relates the applied differential stress (σ_{diff}, i.e., the difference between the maximum and minimum principal stresses) to the shear stress resolved on the slip/twin system (τ^s) by

$$\tau^s = m^s\sigma_{\text{diff}}. \quad (2)$$

The maximum fraction of the differential stress (σ_{diff}) that can be resolved onto a slip/twin plane in the slip/twin direction is 0.5. This corresponds to the maximum value of m^s.

An alternative approach, which allows analysis of varied stress states, is to employ the Schmid tensor. The symmetric Schmid tensor ($\mathbf{m^s}$) describes the projection of the deviatoric stress tensor ($\boldsymbol{\sigma}$, i.e., with the mean stress subtracted from each normal stress) onto a slip/twin system (s), defined by unit vectors describing a slip/twin direction ($\mathbf{b}^s$) and slip/twin plane normal ($\mathbf{n}^s$), by

$$\tau^s = \frac{1}{2}(\mathbf{b}^s \otimes \mathbf{n}^s + \mathbf{n}^s \otimes \mathbf{b}^s) : \boldsymbol{\sigma} = \mathbf{m}^s : \boldsymbol{\sigma}, \quad (3)$$

which yields the shear stress resolved on that slip system (τ^s) (for a recent review, see Pokharel *et al*., 2014). In other words, the components of $\mathbf{m^s}$ determine the fraction of each component in the deviatoric stress tensor that is resolved onto the slip/twin plane in the slip/twin direction. In plastically deforming crystals, dislocation glide or twinning can only occur when τ^s exceeds a threshold value, that is, the critical resolved shear stress (τ_c^s) (Schmid, 1928; Schmid and Boas, 1950). The value of τ_c varies with slip/twinning system, material, and environmental conditions, primarily temperature (e.g. De Bresser and Spiers, 1997; Morales *et al*., 2014).

253 To calculate Schmid factors for past deformations, constraints on the palaeo-stress state
254 are required. Differential stresses applied to sample EM1 have been estimated from
255 palaeopiezometric analyses (Table 1; Rutter *et al*., 2007), but the shape of the stress tensor also
256 needs to be determined. Based on the macroscopic kinematics of the Pangong strand, along
257 with asymmetric deformation microstructures and distributions of foliations, lineations, and
258 palaeostress orientations reported by Rutter *et al*. (2007) (Figure 1), we infer that the
259 deformation history of EM1 was dominated by simple shear. To further test the hypothesis that
260 deformation was dominantly simple shear, we apply the approach of Michels *et al*. (2015) to
261 determine the macroscopic vorticity axis from crystallographic orientation data. This method
262 uses principal geodesic analysis of intragranular orientation dispersion to fit a single
263 'crystallographic vorticity axis' (CVA) to each grain. For samples in which dislocation activity
264 accommodated significant strain, CVAs averaged over many grains may record the vorticity
265 axis of deformation.

266 Values of the scalar Schmid factor, m^s, can be computed by entering a normalised stress
267 tensor, $\hat{\boldsymbol{\sigma}}$, in the right hand side of Equation 3 to give

$$m^s = \mathbf{m}^s : \hat{\boldsymbol{\sigma}}. \quad (4)$$

268 Assuming macroscopic simple shear deformation within the Pangong strand, and defining $\hat{\boldsymbol{\sigma}}$ as

$$\hat{\boldsymbol{\sigma}} = \boldsymbol{\sigma}/\sigma_{\text{diff}}, \quad (5)$$

269 gives

270

$$\hat{\boldsymbol{\sigma}} = \begin{bmatrix} 0 & 1/2 & 0 \\ 1/2 & 0 & 0 \\ 0 & 0 & 0 \end{bmatrix}. \quad (6)$$

271 This formulation denotes that the maximum possible value of the shear stress components is
272 half the magnitude of the applied differential stress. This approach is equivalent to that of Law
273 *et al*. (1990), except that they normalised the shear stress components by their maximum

possible magnitude, which leads to non-zero terms in $\hat{\boldsymbol{\sigma}}$ having a value of one and m with values in the range 0–1. In contrast, by normalising the shear stress components by the magnitude of the differential stress, we obtain values of m in the conventional range 0–0.5, which can be used more directly in conjunction with differential stress magnitudes from palaeopiezometry. If crystal orientations can be mapped across the microstructure and the differential stress measured or inferred, then the scalars τ^s and m^s can be mapped across the microstructure.

To determine which of the calcite slip systems could potentially be activated by the palaeostresses, we transform the normalised stress tensor, $\hat{\boldsymbol{\sigma}}$, in Equation 6, into the crystal coordinate system of each measured orientation and compute $\boldsymbol{m^s}$ for each slip system. This stress tensor, $\hat{\boldsymbol{\sigma}}$, and Schmid tensor, $\boldsymbol{m^s}$, allow calculation of m^s by Equation 4. Values of m^s are multiplied by σ_{diff} to calculate the corresponding shear stress, τ^s, resolved on each slip system according to Equation 2. In crystals with multiple symmetrically equivalent variants of each slip/twin system, such as calcite, the variant with the highest value of m^s will slip/twin at the lowest applied stresses.

Once the Schmid factor and resolved shear stress for each slip system have been calculated, it is necessary to assess whether the applied stress was sufficient to activate dislocation glide, i.e., whether $\tau^s > \tau_c^s$. The experimental work on calcite single crystals and data compilation of De Bresser and Spiers (1993, 1997) established the operative calcite slip and twinning systems and their absolute CRSSs over the temperature range 20–800°C. Therefore, we take the values of τ_c for $\{e\}$-twinning and dislocation slip on the $\{r\}$- and $\{f\}$-planes, for temperatures of 200°C and 300°C, from De Bresser and Spiers (1997) (Table 2). These temperatures approximately correspond to the lower- and upper-bounds for temperature constrained by the geological context (Section 2), for the occurrence of twinning and dynamic recrystallisation respectively in sample EM1. We use values of τ_c for the variant of the $\{f\}$ slip system active at ≤ 300°C (i.e., {-1012}<2-201>), rather than the variant active at ≥ 500°C (i.e.,

{-1012}<-101-1>) in the experiments of De Bresser and Spiers (1997). These experiments demonstrated that values of τ_c for calcite slip systems depend little on strain rate (stress exponents in the range 5.3–42.6), which reduces the uncertainty associated with applying them to analyse deformation that occurred at lower strain rates than the deformation experiments. The range of values of τ_c for slip on the $\{r\}$ system at 300°C, reported by De Bresser and Spiers (1997), is on the order of 20 MPa. As this range is smaller than the uncertainties of the palaeopiezometric stress estimates for the nature samples (30–35 MPa, Table 1, Rutter *et al.*, 2007), we consider only the best-fit values of τ_c at each temperature, interpolated from the fits reported by De Bresser and Spiers (1997), to make simple first-order comparisons. From the critical resolved shear stresses constrained by experiments (De Bresser and Spiers, 1997) and from the applied differential stresses constrained by palaeopiezometry (Rutter *et al.*, 2007), we compute the minimum value of m^s (i.e. m_{min}) necessary to initiate twinning or dislocation glide on each system by

$$m_{\min} = \tau_c/\sigma_{\text{diff}}, \quad (7)$$

(Table 2).

Table 2 *Summary of slip system information for EM1*

Deformation temperature (°C)	Slip system	τ_c (MPa)	Applied differential stress (MPa)	Minimum *m* for twinning/dislocation glide
300	$\{e\}$-twinning {-1018}<40-41>	2	98 ± 35	0.02
300	$\{r\}$-slip {10-14}<-2021>	22	98 ± 35	0.22
300	{f}-slip {-1012}<2-201>	52	98 ± 35	0.53
200	$\{e\}$-twinning {-1018}<40-41>	3	210 ± 30	0.01
200	$\{r\}$-slip	41	210 ± 30	0.20

	{10-14}<-2021>			
200	{f}-slip	77	210 ± 30	0.37
	{-1012}<2-201>			

By computing maps of m^s, we are able to determine which grains have $m > m_{min}$ (and $\tau^s > \tau_c^s$) and therefore estimate the area fraction of grains that can deform by each deformation mode under the applied palaeostress conditions. We also perform this analysis for applied stresses throughout the range 1–250 MPa to explore the effects of increasing stress acting on the mapped microstructure at 300°C and 200°C. An MTEX script to carry out these procedures is included as Supplementary Material.

An important caveat to the analysis described here is that the stress state would need to be homogeneous throughout the material for the point-by-point Schmid factors to be reliably accurate. However, micromechanical models of viscoplastic deformation that explicitly account for detailed microstructures suggest that stress and strain vary significantly among grains and are even distributed heterogeneously within grains (e.g. Pokharel *et al*., 2014). Heterogeneous distributions of stress and strain arise due to the elastic and plastic anisotropy of individual grains and local grain-grain interactions. Such heterogeneities have been recently observed in experimentally deformed Carrara marble (Quintanilla-Terminel and Evans, 2016). Thus, rather than interpreting the behaviour of specific individual points or grains, we take the approach of considering the distribution of Schmid factors and predicted slip/twin system activity over ~2500 grains, providing an averaged estimate of the slip system activity across the bulk material. We suggest that these averaged values of slip system activity are more reliable than the results for individual grains displayed in the maps because the stress states averaged throughout the rock volume must equal the macroscopic applied stress state. The Schmid factor approach offers a simple method to consider a larger number of grains than

would be possible using more advanced computational techniques that include stress heterogeneity.

During progressive deformation, Schmid factors define only an instantaneous relationship between stress and crystal orientation, as ongoing crystal rotations continuously modify the Schmid factors for each slip system in aggregates deforming by dislocation glide. Therefore, Schmid factors calculated from the microstructure of an exhumed rock indicate which slip systems would have been well aligned for dislocation glide during the *next* increment of slip (which *ipso facto* never occurred). In contrast, use of mapped Schmid factors to interpret prior deformation that led to formation of the observed microstructure is more complex and requires additional assumptions/constraints regarding microstructural evolution (particularly grain rotations) or steady state. Therefore, Schmid factor analysis is well suited to our application, in which the mylonitic microstructure records a snapshot formed at ~300°C as the dislocation-mediated processes that formed it ceased to operate, and in which our aim is to investigate the controls on the *subsequent* evolution of deformation processes.

4. Results

The measured CPO is consistent with the inference of simple shear deformation. Calcite {*c*}, {*e*} and {r} poles are clustered in point maxima near the foliation normal, whereas the twin and slip directions are weakly girdled with superimposed point maxima close to the lineation direction (Figure 3). The CPO of {f} planes is weak, with three low intensity maxima (Figure 3b).

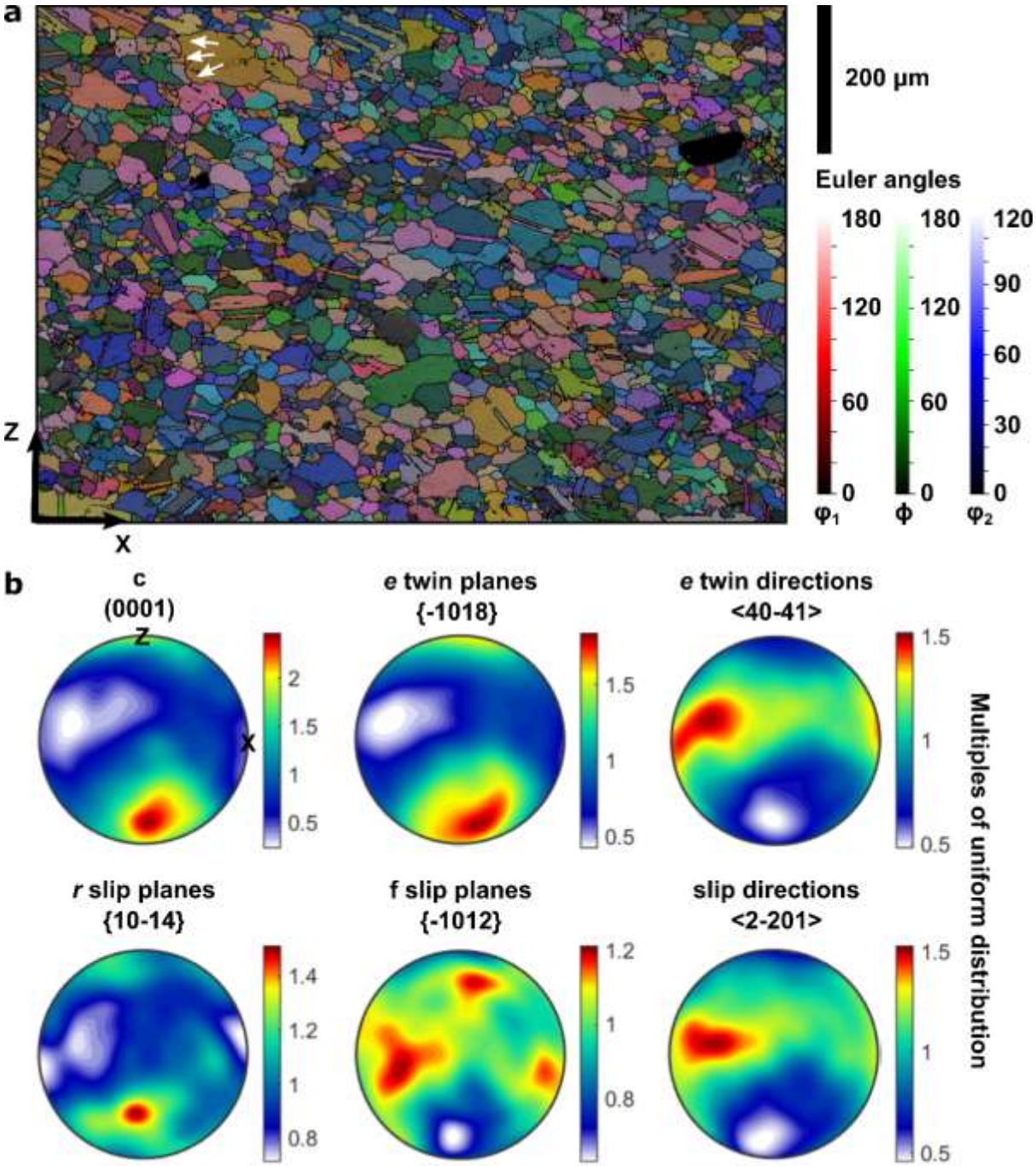

Figure 3 *Crystal orientation data from EBSD analysis of sample EM1. (a) Map of crystal orientations colour-coded using Euler angles in the convention of Bunge (1982), superimposed on a grey-scale map of diffraction pattern band contrast. Black lines mark boundaries of ≥ 10° misorientation between adjacent pixels. White arrows indicate an example of a lobate and irregular grain boundary. (b) Lower hemisphere pole figures of crystal planes and directions*

relevant to the calcite slip and twin systems considered. X indicates the lineation and Z the foliation normal. Shear sense is top-to-right.

Crystallographic misorientation data indicate that relatively few subgrain boundaries with misorientations in the range 1–10° are present (Figure 4a), but the inverse pole figure of misorientation axes demonstrates that those subgrain boundaries that are present have rotation axes parallel to the *a*<11-20> directions (Figure 4b). The map of local misorientations scaled from 0–1.5° reveals the presence of abundant low-angle misorientations of ~1° (Figure 4a). These misorientations are arranged in networks of low-angle subgrain boundaries and regions of more distributed lattice curvature. The portions of grains close to grain boundaries have greater local misorientation relative to the interior, representing higher dislocation densities, than grain interiors (Figure 4a,d). The visible microstructure indicates that the measurements are generally above the background noise level, despite the small misorientation angles. Crystallographic vorticity axes are generally aligned sub-perpendicular to both the lineation and foliation normal, consistent with dominantly simple shear (Figure 4c; Michels *et al*., 2015). This observation provides independent support for our choice of stress state (i.e. Equation 6) used for Schmid factor analysis.

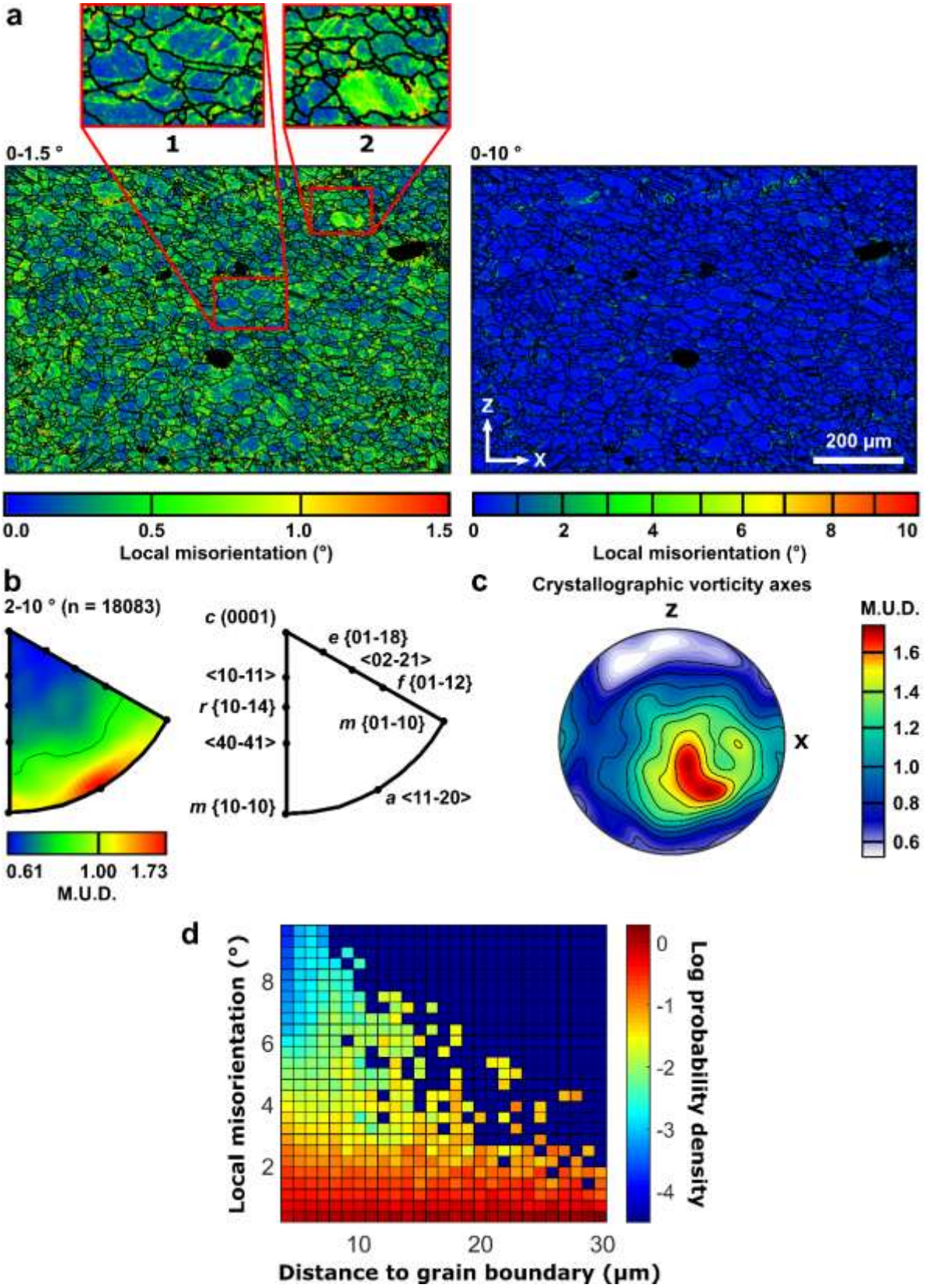

Figure 4 *Misorientation analysis of EM1. (a) Maps of local misorientation within 3x3 pixel kernels, scaled for two ranges of misorientation angle. Grain and twin boundaries are overlaid*

as black lines. Region 1 exhibits higher values of misorientation concentrated near grain boundaries. Region 2 shows both subgrain boundaries (top left) and more widespread misorientation (lower right). (b) Inverse pole figure presents the orientation of misorientation axes of subgrain boundaries in the crystal reference frame. (c) Stereoplot illustrating contoured crystallographic vorticity axes (one axis per grain), determined using the method of principal geodesic analysis of intragranular dispersion (Michels et al., 2015). X indicates the lineation and Z the foliation normal. (d) Probability density functions (PDFs) of local misorientation in 1 µm bins of Euclidean distance to grain boundary (including twin boundaries) within the 2-D EBSD map plane, i.e. each column is a different PDF. This plotting approach addresses the bias of having different numbers of points at each distance by allowing PDFs to be compared between different distances. Local misorientation was calculated within a 3x3 pixel kernel. Only points at distances > 3 µm from a grain boundary are plotted to avoid processing artefacts in kernels that include boundaries. Grain boundaries were defined as >10° misorientation.

Maps of Schmid factor show grain-by-grain variations in the maximum Schmid factor of each family of slip systems (Figure 5). Each family of slip systems exhibits a wide range of Schmid factors within the map area (Figure 5). The probability densities of Schmid factors exhibit similar general form between each slip system, being skewed towards high Schmid factors. The distribution describing Schmid factors for slip on {*f*}-planes is most heavily skewed towards high values (Figure 5). Schmid factors vary between twins and host grains, evident as stripes of different Schmid factor. More subtle variations in Schmid factor are apparent across subgrain boundaries.

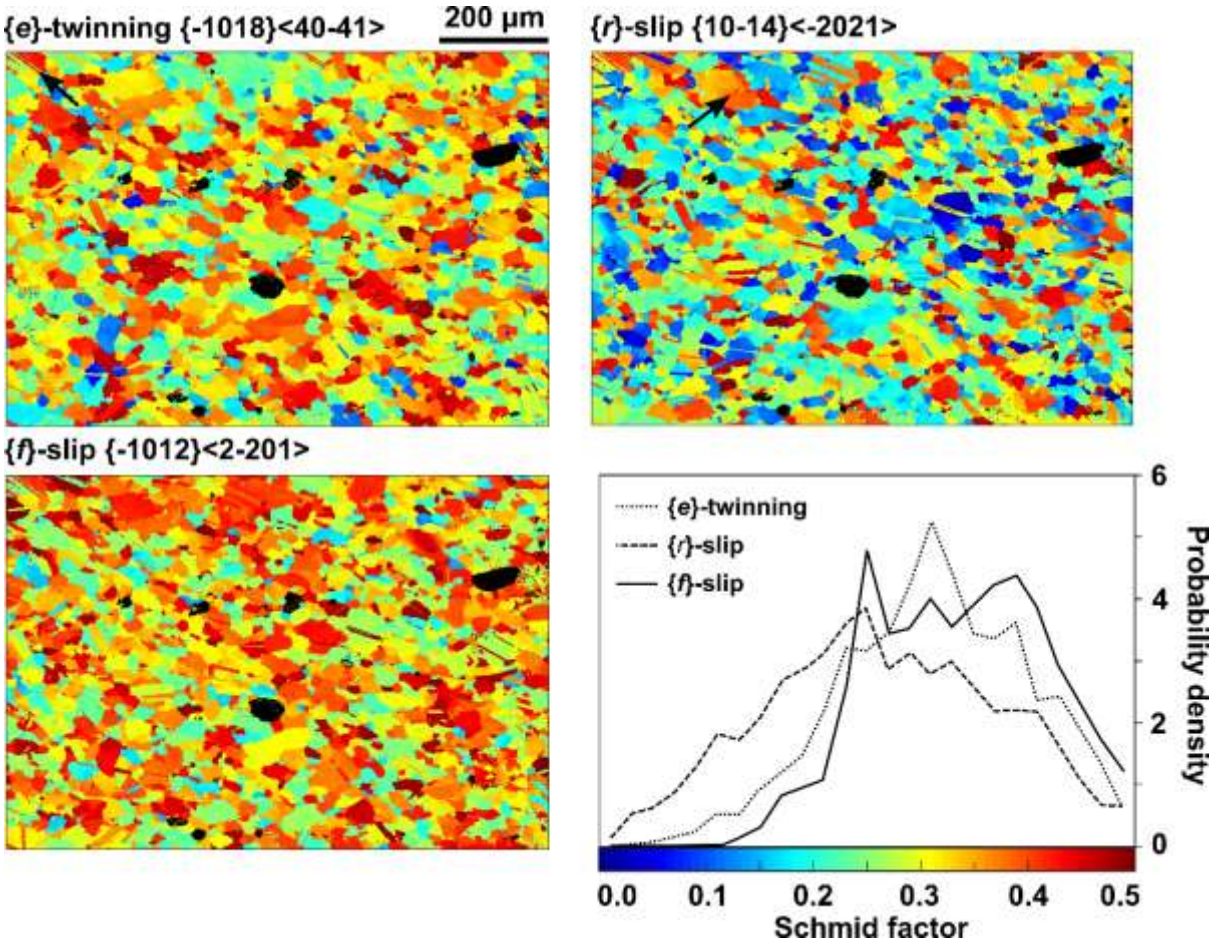

403

404 **Figure 5** *Maps and probability density plots of Schmid factor for each calcite slip/twin system.*
405 *Probability densities were calculated for bins of 0.02 width. The black arrow in the upper-left*
406 *of the map of Schmid factor for {e}-twinning indicates an example of changes in Schmid factor*
407 *across twin boundaries. The black arrow in the upper-left of the map of Schmid factor for {r}-*
408 *slip indicates an example of changes in Schmid factor across a subgrain boundary.*

409 The apparent proportions of grains that can deform by each slip/twin system vary across
410 the temperature and stress ranges within which deformation is inferred to have taken place
411 (figures 6–8). At 300°C and a piezometric stress of 98 MPa, none of the grains can deform by
412 {*f*}-slip because τ_c (52 MPa) is greater than 0.5 of the applied stress (figures 6 and 8a, Table
413 2). However, within the upper-bound uncertainty of the stress estimate, up to 29% of the
414 microstructure can deform by {*f*}-slip (Figure 8a). Within the stress uncertainty, 63 +18/-39%

415 can deform by {*r*}-slip and 100% can deform by {*e*}-twinning (figures 6 and 8a). At 200°C
416 and the higher stress conditions estimated from twinning incidence, 39 +17/-25% should be
417 able to deform by {*f*}-slip and 72 +7/-10% should be able to deform by {*r*}-slip (figures 7 and
418 8b). Again 100% of the grain area exceeds the critical resolved shear stress for {*e*}-twinning
419 (Figures 7 and 8b).

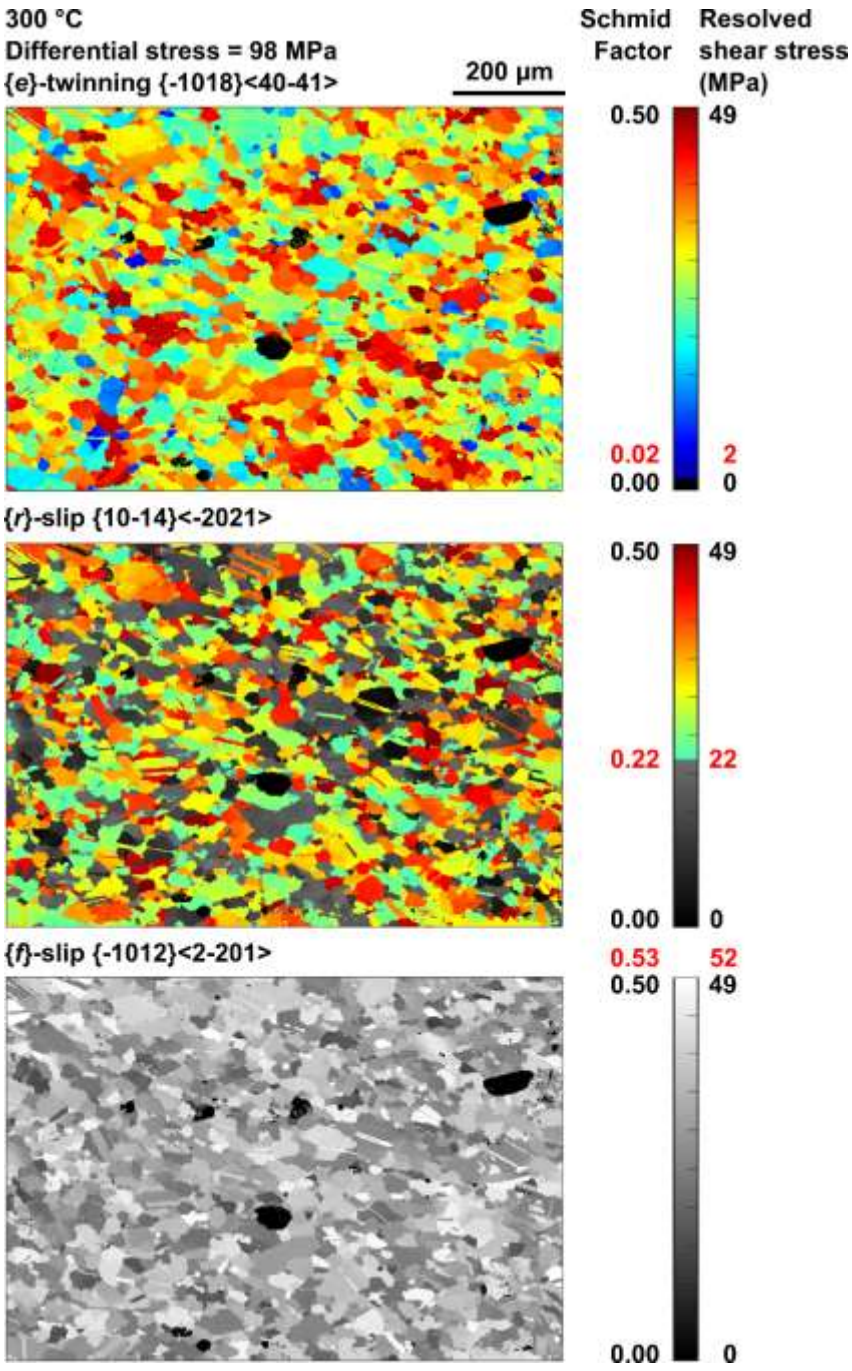

420

421 **Figure 6** *Maps of grains that exceed the minimum Schmid factor necessary to initiate twinning*

or dislocation glide at 300°C and the stress determined from dynamically recrystallised grain size. The minimum Schmid factor and corresponding critical resolved shear stress are marked in red beside the colour bar. Areas above and below this threshold are represented by colour-scale and grey-scale respectively.

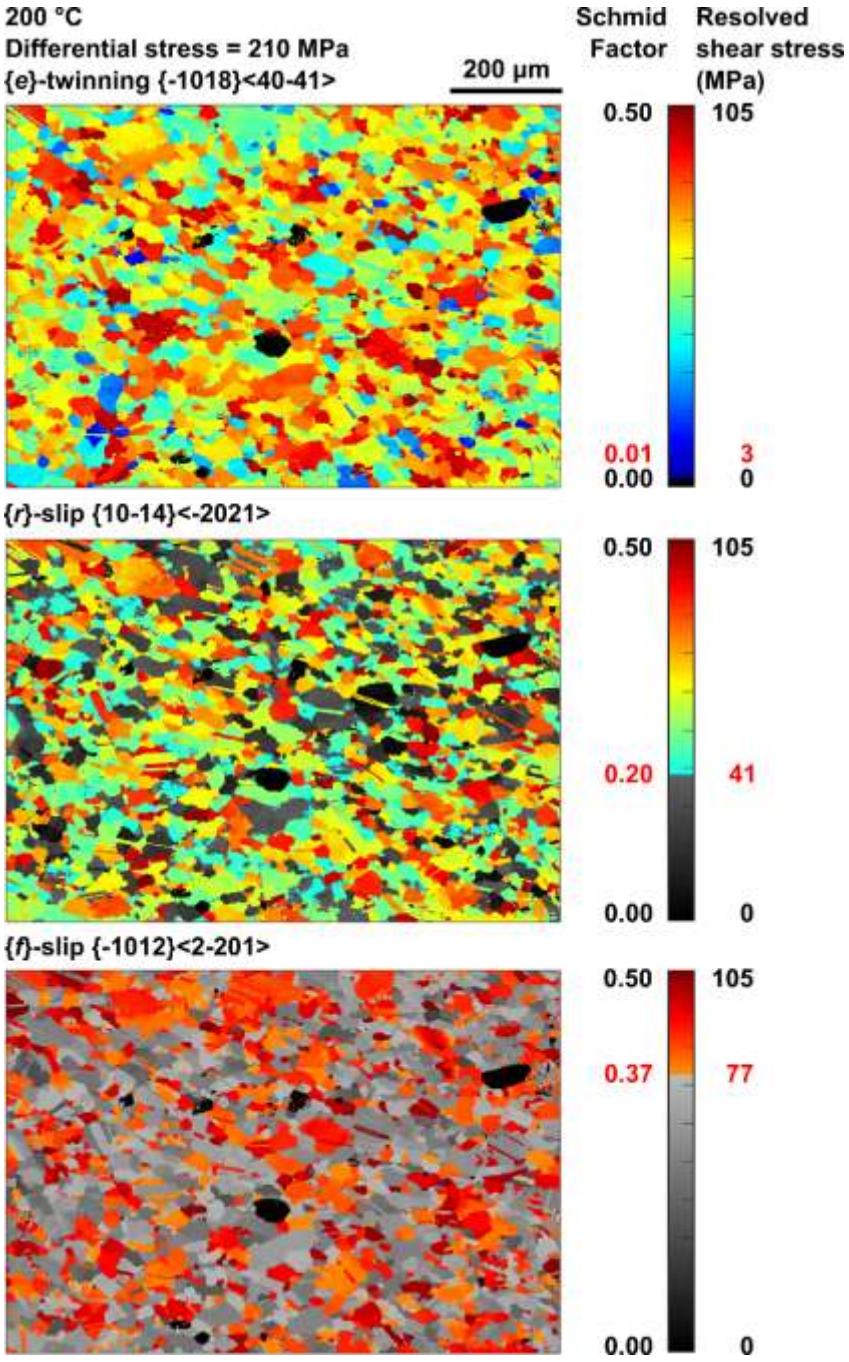

Figure 7 *Maps of grains that exceed the minimum Schmid factor necessary to initiate twinning or dislocation glide at 200°C and the stress determined from twinning incidence. The minimum*

Schmid factor and corresponding critical resolved shear stress are marked in red beside the colour bar. Areas above and below this threshold are represented by colour-scale and grey-scale respectively.

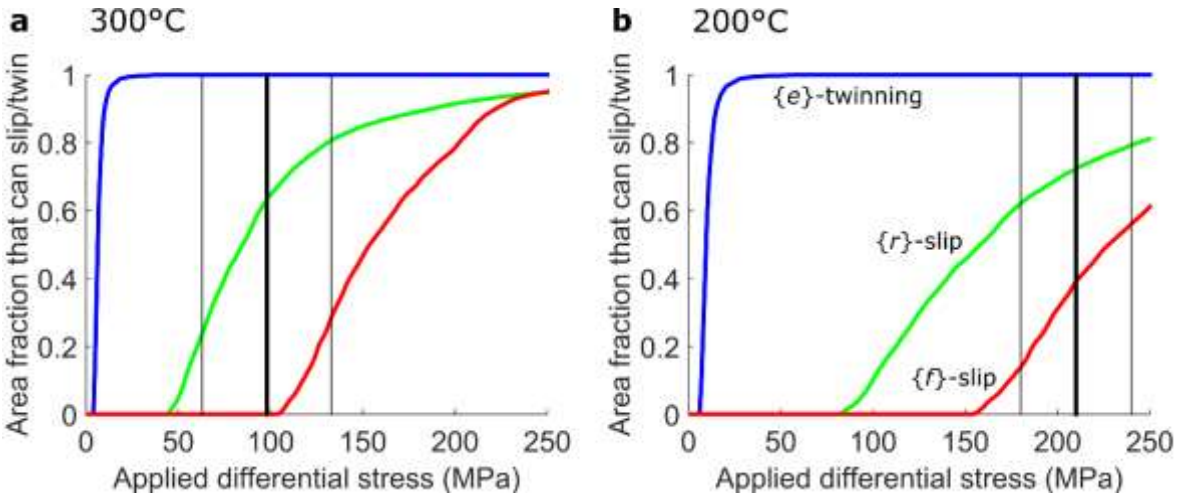

Figure 8 *Area fraction of grains in mapped microstructure that can deform by twinning/dislocation glide at (a) 300°C and (b) 200°C, under applied differential stresses ranging from 0–250 MPa. The stress estimates are determined from (a) dynamically recrystallised grain size (at ~300°C) and (b) twinning incidence (at 200–250°C) and are marked by vertical bold black lines with uncertainties marked by fine black lines.*

5. Discussion

5.1. Effects of changing temperature and stress on slip system activity

This study constitutes a detailed examination of the microstructure of a single sample of marble, EM1, deformed by dislocation glide and twinning whilst the Pangong Metamorphic Complex, within which it was situated, was exhumed through the frictional-viscous transition zone at temperatures of approximately 200–300°C around 7–8 Ma (Rutter *et al.*, 2007; Wallis *et al.*, 2013, 2016b). Although this sample represents only a small volume of the fault zone material, the surrounding rocks, which include a wide range of fault rock types formed under

varied conditions, provide a well-documented context (Rutter *et al*., 2007) in which to interpret the changing styles of deformation in both sample EM1 and the unit as a whole (Figures 1 and 2). In particular, the frictional fault rocks, i.e. marble cataclasites and clay-rich gouge, are more spatially localised than the mylonitic marbles that they overprint (Figure 1; Rutter *et al*., 2007). Therefore, microstructural evidence for earlier deformation mechanisms and processes, such as the recrystallised microstructure indicative of dislocation-mediated deformation in EM1, remains preserved and available for analysis, whilst the subsequent switch to frictional failure of the adjacent rocks can be inferred from the locally overprinting frictional fault rock types. The Kübler index of illite in the clay-rich gouge layer suggests that it formed at up to approximately 300°C and therefore closely post-dated mylonitisation, which ceased at approximately 300°C (Figure 2; Rutter *et al*., 2007). As such, formation of the gouge was broadly coincident with twinning in the mylonitic marbles, which occurred at approximately 200–250°C (Figure 2, Burkhard, 1993). Similarly, the mylonitic marbles are fragmented and overprinted by cataclasites in a zone tens of metres wide adjacent to the gouge layer (Figure 1; Rutter *et al*., 2007). The fragmented marbles contain relict microstructures indicative of partial dynamic recrystallisation by grain boundary migration prior to cataclasis (Rutter *et al*., 2007). Therefore, cataclasis must also have occurred after mylonitisation and been broadly coincident with, or more recent than, formation of the gouge layer and twinning in the mylonites (Figure 2). As the mylonitic fabric of EM1 formed at temperatures similar to or only slightly above those at which frictional deformation commenced in the adjacent rocks, we infer that the mylonitic microstructure of the sample remained largely unmodified during subsequent exhumation. We also note that EM1 is located close to the boundary between the mylonitic and fragmented marbles and therefore is well suited (in both spatial location and timing of formation of its deformation fabric) to recording the transition between dislocation-mediated and frictional deformation. These relationships allow us to examine one sample in detail whilst

471 also considering the significance of the deformation processes in the evolution of the rock unit
472 more widely.

473 The predicted changes in slip system activity in EM1 (Figure 8) reflect the combined
474 influence of changing stress and temperature conditions as the rock was exhumed. The decrease
475 in temperature from 300°C to 200°C increases values of τ_c by factors of 1.5–1.9 (Table 2),
476 acting to inhibit dislocation glide. However, palaeopiezometric estimates suggest that, at the
477 same time, the applied stress increased by a factor of ~2.1 (Rutter *et al*., 2007). As a result, a
478 greater fraction of the microstructure appears to have potential to deform by dislocation glide
479 at 200°C and 210 ± 30 MPa than at 300°C and 98 ± 35 MPa (Figures 6–8). This effect is
480 particularly pronounced for {*f*}-slip, which has the highest τ_c. The 98 ± 35 MPa applied stress
481 at 300°C is generally insufficient for slip on {*f*}-planes, whereas, at 200°C and 210 ± 30 MPa,
482 39 +17/-25% of the microstructure exceeds τ_c for {*f*}-slip (Figure 8). However, these findings
483 are superficially at odds with other microstructural and structural features that indicate
484 dislocation activity was greater at higher temperature. Within the sample, dynamically
485 recrystallised grains formed under the lower stress, higher temperature conditions, and were
486 not overprinted by further dynamic recrystallisation under the subsequent higher stress, lower
487 temperature conditions (Figure 2; Rutter *et al*., 2007). More widely in the rock unit, the
488 mylonitic textures formed at the higher temperatures are overprinted by cataclasites and gouges
489 formed at similar and lower temperatures (Figure 2; Rutter *et al*., 2007). One possible
490 explanation for the discrepancy between the predictions of slip system activity (Figure 8) and
491 the observed (micro)structural evolution is that the stresses predicted from twinning incidence
492 by the palaeopiezometer of Rowe and Rutter (1990) are inaccurate. This method for estimating
493 past stresses is fully empirical and lacks a detailed microphysical basis often used to support
494 application of laboratory-derived relationships to natural contexts. However, the predicted
495 stresses would have to be in error by approximately a factor of two, or approximately 100 MPa,

to preclude slip on the $\{r\}$ system in well oriented grains (Figure 8). Therefore, in the following section, we discuss in more detail the evolution of deformation processes as the rock cooled during exhumation to explore the possibility that microphysical processes are responsible for lack of significant dislocation glide under the low temperature and high stress conditions.

5.2. Evolution of deformation mechanisms during exhumation through the frictional-viscous transition zone

Calcite microstructures in EM1 (this study) and the other samples reported by Rutter *et al*. (2007) include lobate grain boundaries (Figures 3 and 4), porphyroclasts with fine grained mantles (Rutter *et al*., 2007), and subgrain boundaries (Figure 4). These microstructural observations indicate deformation by dislocation motion, accompanied by dynamic recrystallisation due to grain boundary migration and (to a lesser extent) subgrain rotation (Figures 3 and 4; Rutter *et al*., 2007). Crosscutting relationships and contrasting palaeopiezometric estimates indicate that these microstructures formed close to the upper bound temperature of 310 ± 20°C for EM1, constrained by the (now partially overprinted) equilibrium grainsize (Figure 2; Rutter *et al*., 2007).

The general scarcity of subgrain boundaries with misorientations of several degrees or more (Figure 4) indicates that dislocation climb was limited at these temperatures and/or that recovery of intracrystalline strain occurred by other processes, such as cross-slip, dislocation annihilation or climb into high-angle grain boundaries and grain-boundary migration (de Bresser and Spiers, 1990; Liu and Evans, 1997). Misorientation analysis of the few subgrain boundaries that are present indicates that they mostly involve lattice rotations around axes parallel to *a*<11-20>. Bestmann and Prior (2003) demonstrated that misorientation axes parallel to <*a*> in calcite cannot represent twist boundaries due to the lack of appropriate screw dislocation types in calcite. They also suggested that a precisely defined misorientation axis

520 could result from coupled activity of glide in two co-planar directions, but that this is unlikely
521 in general as it requires an equal contribution from both slip directions. Rather, the
522 misorientation axes are consistent with tilt boundaries constructed of edge dislocations on the
523 *r*{10-14}<-2021> or *f*{-1012}<10-11> slip systems (Bestmann and Prior, 2003). However, as
524 *f*{-1012}<10-11> is the high temperature form of {*f*}-slip, active above 500°C in the
525 experiments of De Bresser and Spiers (1997), dislocations on this slip system are unlikely to
526 have formed the subgrain boundaries in EM1. Edge dislocations on the low temperature {*f*}-
527 slip system, *f*{-1012}<2-201>, which we have analysed here, do not generate lattice rotations
528 around <*a*> and therefore also cannot form the subgrain boundaries in EM1. We infer therefore
529 that the subgrain boundaries are constructed of edge dislocations on the *r*{10-14}<-2021> slip
530 system. This interpretation is consistent with the estimate that ~63–72% of the microstructure
531 had sufficient resolved shear stress for slip on *r*{10-14}<-2021> across the range of conditions
532 investigated (Figure 8). These conclusions are similar to those reached by Bestmann and Prior
533 (2003), who investigated calcite deformed at temperatures in the range ~300–350°C.

534 The marble mylonites are sequentially overprinted by more localised marble cataclasite
535 and the clay-bearing gouge zone (Figures 1 and 2; Rutter *et al.*, 2007). These cross-cutting
536 relationships and associated microstructures indicate that, as temperature decreased during
537 exhumation, stress increased sufficiently that the frictional failure strength of the rock was
538 exceeded. This onset of frictional deformation occurred after mylonitisation at ~300°C and
539 before, or broadly coincident with, development of the preserved set of twins in the marble
540 (200–250°C, Figure 2; Rutter *et al.*, 2007). We provide additional insight through our Schmid
541 factor analysis, which demonstrates that the calcite would still have had sufficient resolved
542 shear stress for dislocation glide in most crystal orientations *if* CRSS values taken from the
543 yield points in single crystal experiments are applicable to the natural microstructure. The
544 resolved shear stress appears sufficient for considerable dislocation glide even at the lower

545 temperatures of 200–250°C (Figures 7 and 8) at which only twinning and frictional failure
546 occurred (Rutter *et al.*, 2007). In fact, the predictions of slip system activity (Figure 8) indicate
547 that the applied shear stress would have to have been approximately half of the value measured
548 by twinning incidence to de-activate $\{r\}$-slip in a significant portion of the microstructure.

549 It is important to note that the τ_c values upon which this analysis is based were
550 experimentally determined for relatively low strains of just a few percent ($\leq 4.3\%$, De Bresser
551 and Spiers, 1997). De Bresser and Spiers (1997) recognized significant strain hardening in their
552 experiments, such that the CRSS obtained from yield point stresses effectively places a
553 minimum bound on the resolved shear stress required for further dislocation glide on the
554 corresponding slip system at higher strains. This observation led De Bresser and Spiers (1997)
555 to suggest that strain hardening on the first slip system to activate (i.e., $\{r\}$-slip) could lead to
556 a strain-induced transition to a different dominant slip system (e.g., $\{f\}$-slip).

557 Strain hardening in calcite during cooling is likely the result of a reduction in the
558 efficiency of thermally activated intracrystalline strain recovery processes such as cross slip or
559 dislocation climb into either static or migrating twin, subgrain, and grain boundaries (Rutter,
560 1974; De Bresser and Spiers, 1990; Kennedy and White, 2001). As a result, dislocation
561 interactions and long-range stress fields associated with accumulations of blocked dislocations
562 would have inhibited further dislocation glide (Fleck *et al.*, 1994; Renner *et al.*, 2002). Two
563 lines of microstructural evidence support this interpretation. The widespread occurrence of
564 subgrain boundaries with low misorientation angles of approximately 0.5–1.0° (Figure 4)
565 suggests that significant dislocation content is present but that dislocations could not organise
566 into lower-energy structures. Similarly, misorientation angles, and hence dislocation content,
567 generally increase towards grain boundaries (Figure 4) suggesting that dislocation climb into
568 boundaries and grain-boundary migration were relatively inefficient compared to the rate of

569 dislocation accumulation.

570 Renner *et al*. (2002) suggested that calcite commonly exhibits a Hall-Petch relationship
571 whereby strength increases with decreasing grain size because back-stresses from dislocations
572 accumulated near grain boundaries inhibit further dislocation glide. This model is consistent
573 with the microstructural observations (orientation gradients generally increasing towards grain
574 boundaries) and mechanical inferences (occurrence of strain hardening) of this study. Kennedy
575 and White (2001) reached similar conclusions based on observations of calcite naturally
576 deformed at relatively low temperatures of 150–250°C. Microstructures in their samples
577 indicated that coarse-grained vein calcite that crystallised with low dislocation densities was
578 able to deform by dislocation glide, whereas finer-grained mylonitic matrix exhibited high
579 densities of tangled dislocations and was interpreted to have strain-hardened. We suggest
580 therefore that the transition from dislocation-mediated flow to frictional failure was promoted
581 by work hardening due to low efficiency of recovery processes, particularly slow climb into
582 grain boundaries, rather than simply the temperature-dependency of critical resolved shear
583 stresses, as the rocks cooled during exhumation. This inference is consistent with experimental
584 observations that strain hardening is more pronounced at lower temperatures for both single
585 crystals (de Bresser and Spiers, 1993, 1997) and aggregates (Rutter, 1974). The predictions of
586 slip system activity (Figure 8) suggest that strain hardening must have imposed additional
587 resistance to glide of at least tens of MPa to prevent large fractions of the microstructure
588 deforming by $\{r\}$-slip.

589 Microstructures indicative of frictional deformation are preserved within both the
590 cataclastic marbles and the phyllosilicate-rich gouge band (Figure 1; Rutter *et al*., 2007). As
591 Quaternary earthquakes of magnitude 7+ are recorded by offset alluvial fans and debris flows
592 within 2 km of the sample site (Brown *et al*., 2002; Rutter *et al*., 2007), it is pertinent to consider

593 the extent to which the exhumed cataclastic fault rocks record seismogenic processes as an
594 analogue for those occurring at depth. Phyllosilicate-rich gouges typically exhibit velocity-
595 strengthening behaviour and therefore are unfavourable in general for nucleation of earthquake
596 ruptures (Ikari *et al*., 2011). However, carbonate rocks exhibit strong velocity weakening (Han
597 *et al*., 2010), and therefore the fragmented marble band was likely capable of nucleating
598 unstable earthquake ruptures whilst at depth. In this case, one important consequence of strain
599 hardening may be to result in the onset of seismogenic deformation at the structural levels at
600 which rocks are exhumed and cooled from ~300°C to ~200–250°C. We suggest that the
601 processes recorded in the presently exposed fault rocks of the Pangong strand are likely
602 analogous to those occurring at depth, where similar rocks of the PMC continue to be exhumed
603 through the frictional-viscous transition zone.

604 In the case of the KFZ, cooling through the frictional-viscous transition zone was due
605 to ongoing deformation during erosional exhumation (Wallis *et al*., 2016b). However, the
606 processes documented in this study may also be important in controlling transitions in
607 deformation mechanism and the onset of seismogenic behaviour in other tectonic settings. In
608 particular, carbonate units are commonly dissected by extensive normal fault systems in which
609 tectonic exhumation of footwalls may contribute to cooling (Smith *et al*., 2011; Cowie *et al*.,
610 2017). The processes of strain hardening leading to frictional failure may be important controls
611 on the depth of seismicity and strength of the extending mid-crust in such settings. An
612 implication of this finding is that the depth extent of the dominantly frictional upper crust,
613 where earthquakes typically nucleate, potentially varies in both space and time in response to
614 the evolving strain state of rocks in the mid-crust.

615 **5.3. Schmid factor analysis as a tool for analysing crystal plasticity**

616 Schmid-factor analysis provides several useful insights in addition to those that can be

gained from more commonly used methods of slip system analysis. Schmid factor maps provide an extension of common CPO analysis by allowing populations of crystal orientations to be readily related directly to specific microstructural elements (e.g. Figures 5–7). This approach is similar to plotting EBSD maps colour-coded using inverse pole figures, except that Schmid factor maps consider the complete crystallography (i.e. angular relationships involving both the slip direction and slip plane normal) rather than individual crystal directions, and relate this explicitly to a stress state of interest (which is often only implied in other approaches).

Schmid factor mapping is also the first step to more detailed quantitative analysis of slip system activity, which requires a range of geological (e.g. stress and temperature) and experimental (e.g. CRSS and strain rate sensitivity) constraints. In these respects, calcite is ideal, whereas other common rock forming minerals may present additional challenges. For example, the slip systems of quartz are relatively well constrained and quartz slip system analysis is widely applied in studies of crustal deformation (e.g. Law *et al.*, 1990; Lloyd *et al.*, 1997; Morales *et al.*, 2014). However, single crystals of quartz exhibit complex yield behaviour, with strength dependent not only on temperature but also strain rate and intragranular water content (Hobbs *et al.*, 1972). Consequently, comprehensive measurements of slip system strength, such as those available for calcite (de Bresser and Spiers, 1997), are not currently available for quartz. As a result of these limitations, although it is possible to calculate Schmid factors for quartz slip systems, it is not yet possible to infer which slip systems have sufficient resolved shear stress for slip. Similar detailed considerations must be applied to other common rock-forming minerals.

More generally, Schmid factor analysis can require a range of assumptions, depending on the application, which must be critically evaluated. In the present work we are concerned with why dislocation activity ceased at the time that the preserved mylonitic microstructure

641 was formed. In this respect, Schmid factor analysis is highly appropriate because it constrains
642 which slip systems were well aligned for dislocation glide during a hypothetical *future*
643 increment of dislocation-mediated strain. However, a common objective of other rock
644 deformation studies is to interpret how an observed microstructure formed in the first place.
645 Schmid factors calculated for specific points/grains in a mapped microstructure will generally
646 not equal those present during *prior* deformation that lead to formation of the observed
647 microstructure due to microstructural evolution (e.g., grain rotation, grain boundary migration).
648 In some instances, this limitation might be overcome by assuming that the microstructure had
649 'on average' reached a steady state, in combination with analysing Schmid factor distributions
650 over a large portion of the microstructure. However, microstructural steady state, and in
651 particular steady-state CPO, can require shear strains of several hundred percent and can be
652 difficult to prove (Skemer and Hansen, 2016). Averaging over large portions of the
653 microstructure also provides the benefit of reducing the influence of inter- and intra-granular
654 stress heterogeneities. Such heterogeneities have been predicted by numerical modelling (e.g.,
655 Pokharel *et al.*, 2014; Lebensohn and Needleman, 2016) and documented in geological
656 crystalline aggregates, including calcite (Quintanilla-Terminel and Evans, 2016) and quartz
657 (Chen *et al.*, 2015), and even in single crystals of olivine (Wallis *et al.*, 2017). Therefore, it is
658 important to map Schmid factors over a sufficiently large portion of the microstructure that the
659 averaged internal stress state can be reasonably expected to have approached the macroscopic
660 externally applied stress state during deformation. Notwithstanding these caveats, the present
661 study demonstrates that Schmid factor analysis can provide geologically relevant information,
662 if used in conjunction with appropriate objectives and geological constraints.

663 **6. Conclusions**

664 Schmid factor analysis indicates that calc-mylonites in the Pangong strand of the KFZ
665 deformed primarily by dislocation glide on *r*{10-14}<-2021> at ~300°C and 98 ± 35 MPa

666 differential stress (Rutter *et al*., 2007) and by e{-1018}<40-41> twinning at similar and lower
667 temperatures. In contrast, the critical resolved shear stress for dislocation glide on *f*{-1012}<2-
668 201> precluded this slip system from activating in the majority of grains under the same
669 conditions. Deformation within the Karakoram Fault Zone continued as the rocks cooled during
670 exhumation, resulting in hardening of the calc-mylonites and thereby leading to a transition
671 from crystal plastic to frictional deformation mechanisms (Rutter *et al*., 2007, Wallis *et al*.,
672 2013). One mechanism for such hardening is by the direct temperature effect of increasing
673 critical resolved shear stresses of the active slip and twin systems (De Bresser and Spiers,
674 1997). However, Schmid factor analysis indicates that this alone was insufficient to induce
675 frictional failure as a greater fraction of the microstructure apparently had sufficient resolved
676 shear stress for dislocation glide at 200°C than at 300°C. Instead, microstructural observations,
677 such as widespread low angle crystallographic misorientations, which increase towards grain
678 boundaries, indicate that intracrystalline strain recovery was inefficient. Strain hardening, due
679 to decreasing efficiency of recovery as temperature decreased, provides an additional
680 hardening mechanism, which we interpret as having led to the onset of frictional and potentially
681 seismogenic deformation in the rocks at this structural level. These findings highlight the
682 importance of detailed understanding of the interplay of strain hardening and recovery
683 processes for models of crystal plasticity, particularly at relatively low homologous
684 temperatures where they impact the transition to frictional and potentially seismogenic
685 deformation.

686 **Acknowledgements**

687 We thank Richard Phillips and Ernie Rutter for providing the sample for this study,
688 Cees Passchier for his editorial handling of the manuscript, and Hans de Bresser and Elisabetta
689 Mariani for their reviews. We are grateful to Rick Law, Gordon Lister and Andrew Turner for
690 helpful discussions. David Wallis and Lars Hansen acknowledge support from the Natural

691 Environment Research Council grant NE/M000966/1. Data reported in this study are available
692 on request from the corresponding author.

693 **References**

694 Bachmann, F., Hielscher, R., Schaeben, H., 2010. Texture Analysis with MTEX – Free and
695 Open Source Software Toolbox. Solid State Phenomena, 160, 63–68, doi:
696 10.4028/www.scientific.net/SSP.160.63.

697 Bestmann, M., Prior, D.J., 2003. Intragranular dynamic recrystallisation in naturally deformed
698 calcite marble: diffusion accommodated grain boundary sliding as a result of subgrain
699 rotation recrystallisation. Journal of Structural Geology, 25, 1597–1613, doi:
700 10.1016/S0191-8141(03)00006-3.

701 Bestmann, M., Prior, D.J., Grasemann, B., 2006. Characterisation of deformation and flow
702 mechanics around porphyroclasts in a calcite marble ultramylonite by means of EBSD
703 analysis. Tectonophysics 413, 185–200, doi: 10.1016/j.tecto.2005.10.044.

704 Boutonnet, E., Leloup, P.H., Arnaud, N., Paquette, J.-L., Davis, W.J., Hattori, K., 2012.
705 Synkinematic magmatism, heterogeneous deformation, and progressive strain
706 localisation is a strike-slip shear zone: The case of the right-lateral Karakorum fault.
707 Tectonics 31, TC4012, doi: 10.1029/2011TC003049.

708 Brown, E.T., Bendick, R., Bourlès, D.L., Gaur, V., Molnar, P., Raisbeck, G.M., Yiou, F, 2002.
709 Slip rates of the Karakorum fault, Ladakh, India, determined using cosmogenic ray
710 exposure dating of debris flows and moraines. Journal of Geophysical Research 107,
711 B9, 2192, doi: 10.1029/2000JB00100.

712 Bunge, H., 1982. Texture Analysis in Materials Science: Mathematical Models. Butterworths,
713 London, pp. 614.

714 Burkhard, M., 1993. Calcite twins, their geometry, appearance and significance as stress-strain
715 markers and indicators of tectonic regime: a review. Journal of Structural Geology 15,
716 351–368, doi: 10.1016/0191-8141(93)90132-T.

717 Chen, K., Kunz, M., Tamura, N., Wenk, H.-R., 2015. Residual stress preserved in quartz from
718 the San Andreas Fault Observatory at Depth. Geology 43, 219–222, doi:
719 10.1130/G36443.

720 Covey-Crump, S.J., Rutter, E.H., 1989. Thermally induced grain growth of calcite marbles on
721 Naxos Island, Greece. Contributions to Mineralogy and Petrology 101, 69–86, doi:
722 10.1007/BF00387202.

723 Cowie, P.A., Phillips, R.J., Roberts, G.P., McCaffrey, K., Zijerveld, L.J.J., Gregory, L.C.,
724 Faure Walker, J., Wedmore, L.N.J., Dunai. T.J., Binnie, S.A., Freeman, S.P.H.T.,
725 Wilcken, K., Shanks. R.P., Huismans, R.S., Papanikolaou, I., Michetti, A.M.,
726 Wilkinson, M., 2017. Orogen-scale uplift in the central Italian Apennines drives
727 episodic behaviour of earthquake faults. Scientific Reports 7, 44858, doi:
728 10.1038/srep44858.

729 De Bresser, J.H.P., Spiers, C.J., 1990. High temperature deformation of calcite single crystals
730 by r^+ and f^+ slip. In: Knipe, R.J., Rutter, E.H. (Eds.) Deformation Mechanisms,
731 Rheology and Tectonics. Geological Society, London, Special Publications 54, 285–
732 298, doi: 10.1144/GSL.SP.1990.054.01.25.

733 De Bresser, J.H.P., Spiers, C.J., 1993. Slip systems in calcite single crystals deformed at 300–
734 800°C. Journal of Geophysical Research 98, 6397-6409, doi: 10.1029/92JB02044.

735 De Bresser, J.H.P., Spiers, C.J., 1997. Strength characteristics of the *r*, *f*, and *c* slip systems in
736 calcite. Tectonophysics 272, 1–23, doi: 10.1016/S0040-1951(96)00273-9.

737 Farla, R.J.M., Fitz Gerald, J.D., Kokkonen, H., Halfpenny, A., Faul, U.H., Jackson, I., 2011.
738 Slip system and EBSD analysis on compressively deformed fine-grained
739 polycrystalline olivine. In: Prior, D.J., Rutter, E.H., Tatham, D.J. (Eds.) Deformation
740 Mechanisms, Rheology and Tectonics: Microstructures, Mechanics and Anisotropy.
741 Geological Society, London, Special Publications 360, 225–235, doi:
742 10.1144/SP360.13.

743 Fleck, N.A., Muller, G.M., Ashby, M.F., Hutchinson, J.W., 1994. Strain gradient plasticity:
744 theory and experiment. Acta Metallurgica et Materialia 42, 475–487, doi:
745 10.1016/0956-7151(94)90502-9.

746 Han, R., Hirose, T., Shimamoto, T., 2010. Strong velocity weakening and powder lubrication
747 of simulated carbonate faults at seismic slip rates. Journal of Geophysical Research
748 115, B03412.

749 Handy, M.R., Hirth, G., Bürgmann, R., 2007. Continental fault structure and rheology from the
750 frictional-viscous transition downward. In: Handy, M.R., Hirth, G., Hovius, N. (Eds.)
751 Tectonic Faults – Agents of Change on a Dynamic Earth. The MIT Press, Cambridge,
752 Massachusetts, Dahlem Workshop Report 95, 139–181.

753 Hansen, L.N., Zimmerman, M.E., Kohlstedt, D.L., 2011. Grain boundary sliding in San Carlos
754 olivine: Flow law parameters and crystallographic-preferred orientation. Journal of
755 Geophysical Research 116, B08201, doi: 10.1029/2011JB008220.

756 Hobbs, B.E., McLaren, A.C., Paterson, M.S., 1972. Plasticity of Single Crystals of Synthetic
757 Quartz. In: Heard, H.C., Borg, I.Y., Carter, N.L., Rayleigh, C.B. (Eds.) Flow and
758 Fracture of Rocks. American Geophysical Union, Washington D.C., p. 29–53, doi:
759 10.1029/GM016p0029.

760 Ikari, M.J., Marone, C., Saffer, D.M., 2011. On the relation between fault strength and

761 frictional stability. Geology 39, 83–86, doi: 10.1130/G31416.1.

762 Kennedy, L.A., White, J.C., 2001. Low-temperature recrystallisation in calcite: Mechanisms
763 and consequences. Geology 29, 1027–1030, doi: 10.1130/0091-
764 7613(2001)029<1027:LTRICM>2.0.CO;2.

765 Law, R.D., Schmid, S.M., Wheeler, J., 1990. Simple shear deformation and quartz
766 crystallographic fabrics: a possible natural example from the Torridon area of NW
767 Scotland. Journal of Structural Geology 12, 29–45.

768 Lebensohn, R.A., Needleman, A., 2016. Numerical implementation of non-local polycrystal
769 plasticity using fast Fourier transforms. Journal of the Mechanics and Physics of Solids
770 97, 333–351, doi: 10.1016/j.jmps. 2016.03.023.

771 Liu, M., Evans, B., 1997. Dislocation recovery kinetics in single-crystal calcite. Journal of
772 Geophysical Research 102, 24801-24809, doi: 10.1029/97JB01892.

773 Lloyd, G.E., Farmer, A.B., Mainprice, D., 1997. Misorientation analysis and the formation and
774 orientation of subgrain and grain boundaries. Tectonophysics 279, 55–78, doi:
775 10.1016/S0040-1951(97)00115-7.

776 Mainprice, D., Bachmann, F., Hielscher, R., Schaeben, H., 2011. Calculating anisotropic
777 physical properties from texture data using the MTEX open source package. In: Prior,
778 D.J., Rutter, E.H., Tatham, D.J. (Eds.) Deformation Mechanisms, Rheology and
779 Tectonics: Microstructures, Mechanics and Anisotropy. Geological Society, London,
780 Special Publications 360, 175–192, doi: 10.1144/SP360.10.

781 Michels, Z.D., Kruckenburg, S.C., Davis, J.R., Tikoff, B., 2015. Determining vorticity axes
782 from grain-scale dispersion of crystallographic orientations. Geology 43, 803–806.

783 Morales, L.F.G., Lloyd, G.E., Mainprice, D., 2014. Fabric transitions in quartz via viscoplastic

784 self-consistent modeling part I: Axial compression and simple shear under constant
785 strain. Tectonophysics 636, 52–69.

786 Parsons, A.J., Law, R.D., Lloyd, G.E., Phillips, R.J., Searle, M.P., 2016. Thermo-kinematic
787 evolution of the Annapurna-Dhaulagiri Himalaya, central Nepal: The Composite
788 Orogenic System. Geochemistry, Geophysics, Geosystems 17, 1511–1539, doi:
789 10.1002/2015GC006184.

790 Phillips, R.J., Parrish, R.R., Searle, M.P., 2004. Age constraints on ductile deformation and
791 long-term slip rates along the Karakoram fault zone, Ladakh. Earth and Planetary
792 Science Letters 226, 305–319, doi: 10.1016/j.epsl.2004.07.037.

793 Phillips, R.J., Searle, M.P., 2007. Macrostructural and microstructural architecture of the
794 Karakoram fault: Relationship between magmatism and strike–slip faulting. Tectonics
795 26, TC3017, doi: 10.1029/2006TC001946.

796 Pokharel, R., Lind, J., Kanjarla, A.K., Lebensohn, R.A., Li, S.F., Kenesei, P., Suter, R.M.,
797 Rollett, A.D., 2014. Polycrystal Plasticity: Comparison Between Grain-Scale
798 Observations of Deformation and Simulations. Annual Review of Condensed Matter
799 Physics 5, 317–346, doi: 10.1146/annurev-conmatphys-031113-133846.

800 Prior, D.J., 1999. Problems in determining the misorientation axes, for small angular
801 misorientations, using electron backscatter diffraction in the SEM. Journal of
802 Microscopy 195, 217–225, doi: 10.1046/j.1365-2818.1999.00572.x.

803 Prior, D.J., Boyle, A.P., Brenker, F., Cheadle, M.C., Day, A., Lopez, G., Peruzzo, L., Potts,
804 G.J., Reddy, S., Spiess, R., Timms, N.E., Trimby, P., Wheeler, J., Zetterström, L., 1999.
805 The application of electron backscatter diffraction and orientation contrast imaging in
806 the SEM to textural problems in rocks. American Mineralogist 84, 1741–1759, doi:
807 10.2138/am-1999-11-1204.

808 Prior, D.J., Mariani, E., Wheeler, J., 2009. EBSD in the Earth Sciences: Applications, Common
809 Practice, and Challenges. In: Schwartz, A., Kumar, M., Adams, B., Field, D. (Eds.)
810 Electron Backscatter Diffraction in Materials Science. Springer, Boston, MA, 345–360,
811 doi: 10.1007/978-0-387-88136-2_26.

812 Quintanilla-Terminel, A., Evans, B, 2016. Heterogeneity of inelastic strain during creep of
813 Carrara marble: Microscale strain measurement technique. Journal of Geophysical
814 Research: Solid Earth 121, 5736–5760, doi: 10.1002/2016JB012970.

815 Ralser, S., Hobbs, B.E., Ord, A., 1991. Experimental deformation of a quartz mylonite. Journal
816 of Structural Geology 13, 837–850, doi: 10.1016/0191-8141(91)90008-7.

817 Renner, J., Evans, B., Siddiqi, G., 2002. Dislocation creep of calcite. Journal of Geophysical
818 Research 107, B12, 2364, doi: 10.1029/2001JB001680.

819 Rowe, K.J., Rutter, E.H., 1990. Palaeostress estimation using calcite twinning: experimental
820 calibration and application to nature. Journal of Structural Geology 12, 1–17,
821 10.1016/0191-8141(90)90044-Y.

822 Rutter, E.H., 1974. The influence of temperature, strain rate and interstitial water in the
823 experimental deformation of calcite rocks. Tectonophysics, 22, 311–334, doi:
824 10.1016/0040-1951(74)90089-4.

825 Rutter, E.H., 1995. Experimental study of the influence of stress, temperature and strain on the
826 dynamic recrystallisation of Carrara marble. Journal of Geophysical Research 100,
827 24651–24663, doi: 10.1029/95JB02500.

828 Rutter, E.H., Faulkner, D.R., Brodie, K.H., Phillips, R.J., Searle, M.P., 2007. Rock deformation
829 processes in the Karakoram fault zone, Ladakh, NW India. Journal of Structural
830 Geology 29, 1315–1326, doi: 10.1016/j.jsg.2007.05.001.

831 Schmid, E., 1928. Zn normal stress law. Proceedings of the International Congress on Applied
832 Mechanics, Delft, 1924, P. 342.

833 Schmid, E., Boas, I.W., 1950. Plasticity of Crystals. Chapman and Hall, London, pp. 353.

834 Scholz, C.H., 1988. The brittle-plastic transition and the depth of seismic faulting. Geologische
835 Rundschau 77, 319–328, doi: 10.1007/BF01848693.

836 Skemer, P., Hansen, L.N., 2016. Inferring upper-mantle flow from seismic anisotropy: An
837 experimental perspective. Tectonophysics 668–669, 1–14, doi:
838 10.1016/j.tecto.2015.12.003.

839 Smith, S.A.F., Billi, A., Di Toro, G., Spiess, R., 2011. Principle Slip Zones in Limestone:
840 Microstructural Characterization and Implications for the Seismic Cycle (Tre Monti
841 Fault, Central Apennines, Italy). Pure and Applied Geophysics 168, 2365–2393, doi:
842 10.1007/s00024-011-0267-5.

843 Streule, M.J., Phillips, R.J., Searle, M.P., Waters, D.J., Horstwood, M.S.A., 2009. Evolution
844 and chronology of the Pangong Metamorphic Complex adjacent to the Karakoram
845 Fault, Ladakh: constraints from thermobarometry, metamorphic modelling and U Pb
846 geochronology. Journal of the Geological Society 166, 919–932, doi: 10.1144/0016-
847 76492008-117.

848 Toy, V.G., Prior, D.J., Norris, R.J., 2008. Quartz fabrics in the Alpine Fault mylonites:
849 Influence of pre-existing preferred orientations on fabric development during
850 progressive uplift. Journal of Structural Geology 30, 602–621, doi:
851 10.1016/j.jsg.2008.01.001.

852 Turner, F.J., 1953. Nature and dynamic interpretation of deformation lamellae in calcite of
853 three marbles. American Journal of Science 251, 276–298, doi: 10.2475/ajs.251.4.276.

Van Buer, N.J., Jagoutz, O., Upadhyay, R., Guillong, M., 2015. Mid-crustal detachment beneath western Tibet exhumed where conjugate Karakoram and Longmu-Gozha Co faults intersect. Earth and Planetary Science Letters 413, 144–157, doi: 10.1016/j.epsl.2014.12.053.

Verberne, B.A., Niemeijer, A.R., De Bresser, J.H.P., Spiers, C.J., 2015. Mechanical behavior and microstructure of simulated calcite fault gouge sheared at 20–600°C: Implications for natural faults in limestones. Journal of Geophysical Research: Solid Earth 120, 8169–8196, doi: 10.1002/2015JB012292.

Wallis D., Hansen, L.N., Britton, T.B., Wilkinson, A.J., 2016a. Geometrically necessary dislocations in olivine obtained using high-angular resolution electron backscatter diffraction. Ultramicroscopy 168, 34–45, doi: 10.1016/j.ultramic.2016.06.002.

Wallis D., Hansen, L.N., Britton, T.B., Wilkinson, A.J., 2017. Dislocation interactions in olivine revealed by HR-EBSD. Journal of Geophysical Research: Solid Earth, doi: 10.1002/2017JB014513.

Wallis, D., Phillips, R.J., Lloyd, G.E., 2013. Fault weakening across the frictional-viscous transition zone, Karakoram Fault Zone, NW Himalaya. Tectonics 32, 1227–1246, doi: 10.1002/tect.20076.

Wallis, D., Phillips, R.J., Lloyd, G.E., 2014. Evolution of the Eastern Karakoram Metamorphic Complex, Ladakh, NW India, and its relationship to magmatism and regional tectonics. Tectonophysics 626, 41–52, doi: 10.1016/j.tecto.2014.03.023.

Wallis, D., Lloyd, G.E., Phillips, R.J., Parsons, A.J., Walshaw, R.D., 2015. Low effective fault strength due to frictional-viscous flow in phyllonites, Karakoram Fault Zone, NW India. Journal of Structural Geology 77, 45–61, doi: 10.1016/j.jsg.2015.05.010.

877 Wallis, D., Carter, A., Phillips, R.J., Parsons, A.J., Searle, M.P., 2016b. Spatial variation in
878 exhumation rates across Ladakh and the Karakoram: new apatite fission track data from
879 the Eastern Karakoram, NW India. Tectonics 35,doi: 10.1002/2015TC003943.

880 Wang, Z.-C., Bai, Q., Dresen, G., Wirth, R., Evans, B., 1996. High-temperature deformation
881 of calcite single crystals. Journal of Geophysical Research 101, 20377–20390, doi:
882 10.1029/96JB01186.

883 Wenk, H.-R., Takeshita, T., Bechler, E., Erskine, B.G., Matthies, S., 1987. Pure shear and
884 simple shear calcite textures. Comparison of experimental, theoretical and natural data.
885 Journal of Structural Geology 9, 731–745, doi: 10.1016/0191-8141(87)90156-8.

886 Wheeler, J., Mariani, E., Piazolo, S., Prior, D.J., Trimby, P., Drury, M.R., 2009. The weighted
887 Burgers vector: a new quantity for constraining dislocation densities and types using
888 electron backscatter diffraction on 2D sections through crystalline materials. Journal of
889 Microscopy 233, 482–494, doi: 10.111/j.1365-2818.2009.03136.x.